ARTICLE

Solution-Phase Synthesis of Alloyed $Ba(Zr_{1-x}Ti_x)S_3$ Perovskite and Non-Perovskite Nanomaterials

Received 00th January 20xx,
Accepted 00th January 20xx

DOI: 10.1039/x0xx00000x

Daniel Zilevu, Kennedi M. Miller, Naira Arrykova, Autumn B. Locke, Sidney E. Creutz*

Chalcogenide perovskites, especially $BaZrS_3$ and its related alloys, present a promising alternative to lead halide perovskites for optoelectronic applications due to their reduced toxicity and enhanced stability. However, the elevated temperature conditions necessary for preparing these materials create a barrier to their incorporation into thin-film devices. In this work, we report a solution-phase synthesis of colloidal nanoparticles of titanium-alloyed $BaZrS_3$, $Ba(Zr_{1-x}Ti_x)S_3$. The titanium alloying was achieved using reactive amide precursors in oleylamine solvent, and N,N'-diethylthiourea served as the sulfur source. Our methodology allowed for the synthesis of $Ba(Zr_{1-x}Ti_x)S_3$ nanomaterials at temperatures at or below 300 °C. The resulting nanocrystals exhibited a phase transition from an orthorhombic distorted perovskite structure to a hexagonal non-perovskite phase as the Ti content surpassed x = 0.11, accompanied by a morphological evolution from nanoplatelets to nanohexagons and ultimately nanobars. The UV-Vis-NIR absorption spectra of $BaZr_{1-x}Ti_xS_3$ nanoparticles exhibit increasing low-energy absorption as the Ti^{4+} content is increased. This work contributes to the development of low-temperature synthesis methods for $Ba(Zr_{1-x}Ti_x)S_3$ nanomaterials, offering new potential pathways for materials design of chalcogenide perovskites for advanced optoelectronic applications.

Introduction

Organic-inorganic lead halide perovskite solar cells have attracted substantial attention in recent years, demonstrating a rapid escalation in power conversion efficiency (PCE) from an initial value of 3.8 % in 2009 to 25.7 % in 2023 for single-junction solar cells.[1–6] Their success can be attributed largely to the favorable properties of the perovskite light absorbers, which encompass high carrier mobilities, high absorption coefficients, long carrier lifetimes, and good defect tolerance.[7–10] Nevertheless, the structural stability of perovskite materials such as $CH_3NH_3PbI_3$ remains a significant concern; their degradation is accelerated when exposed to ambient air, elevated temperatures, and electric fields.[11] The vulnerability of halide perovskites to these environmental factors is partly attributed to the ionic character and resulting lability of the metal-halogen bonds; a semiconductor material featuring more covalent bonding may have higher stability. Furthermore the presence of the toxic element Pb presents an additional obstacle for the commercial viability of these materials.

In response to the challenges posed by the toxicity and stability concerns inherent in inorganic-organic lead halide perovskites, a class of ternary chalcogenide materials with the general formula ABQ_3, (A= Ca, Ba, Sr; B = Zr, Hf, Ti; Q= S Se) has been put forth as a promising alternative for optoelectronic and solar cell applications.[12] A subset of the materials in this class are known to take on a stable perovskite structure under some conditions, including $CaZrS_3$, $SrZrS_3$, $BaZrS_3$, $CaHfS_3$, and $BaHfS_3$;[13–15] of these, $BaZrS_3$ has garnered the most interest largely because of its lower observed band gaps, falling within the range of 1.75 to 1.94 eV.[12,13,16–22] While these values make it potentially competitive for solar cell applications, especially in a tandem device with silicon, these band gaps are somewhat higher than the ideal for single-junction solar cells and significantly higher than those accessible with lead halide perovskites. However, theoretical calculations based on density functional theory (DFT) suggest that the band gap of $BaZrS_3$ can be reduced through alloying, either by incorporating 3d cation Ti^{4+} to lower the conduction band minimum (CBM) or by introducing 4p anion Se^{2-} to elevate the valence band maximum (VBM); both of these possibilities have been investigated experimentally as well as computationally.[13,23,24] However, it should be noted that neither $BaTiS_3$ or $BaZrSe_3$ is known to occur in perovskite phase; $BaTiS_3$ crystallizes in a hexagonal ($P6_3/mmc$) phase consisting of one-dimensional chains of edge-sharing TiS_6 octahedra interspersed with Ba^{2+} cations.

While the potential of $BaZrS_3$ and its titanium and selenium-alloyed semiconductor derivatives is indeed intriguing, the advancement and assessment of thin film devices have been notably impeded by the limited availability of low-

[a] *Address here.*
[b] *Address here.*
[c] *Address here.*
† Footnotes relating to the title and/or authors should appear here.
Supplementary Information available: [details of any supplementary information available should be included here]. See DOI: 10.1039/x0xx00000x

temperature deposition methods suitable for producing thin films. Syntheses of these materials, particularly $BaZrS_3$ and its titanium alloys, have historically relied on very high temperatures, incompatible with thin-film device processing.[14,21,25,26] In 1957, Hahn and colleagues[27] were pioneers in synthesizing $BaZrS_3$ powder by annealing binary sulfides at 900 °C for two weeks. Clearfield[28] (1963) also achieved $BaZrS_3$ by sulfurizing $BaZrO_3$ with CS_2 at 950-1200 °C. Improved synthetic approaches allowed $BaZrS_3$ powder to be produced at temperatures as low as 550 °C, employing molten BaS_3 as a flux.[25] Other efforts have focused on preparing $BaZrS_3$ thin films; Surendran *et al*. achieved temperatures below 700 °C through pulsed laser deposition,[29] while Comparotto *et al*. grew $BaZrS_3$ thin films at 600 °C using sputtering and sulfurization.[30,31] More recently, significant advances have been made by Agarwal and Bart in preparing thin films from the solution deposition of molecular precursors, with crystalline thin films of $BaZrS3_3$, $BaTiS_3$, and $BaHfS_3$ produced at temperatures as low as 500 °C.[32,33]

An alternative approach to solution-processed thin film deposition is through the preparation and use of colloidal nanocrystal inks;[34,35] however, until recently, solution-phase syntheses of colloidal $BaZrS_3$ nanocrystals were unknown, possibly due in part to the difficulties associated with preparing chalcogenide compounds of highly oxophilic early transition metal cations.[36] We recently reported the successful solution-phase synthesis of $BaZrS_3$ nanoparticles from metal amide precursors within a temperature range from 275 °C to 365 °C.[37] Similar results were also reported by the Hages group, who used barium and zirconium dithiocarbamate precursors to produce $BaZrS_3$ nanoparticles through solvothermal decomposition in oleylamine at 350 °C.[25] The $BaZrS_3$ nanoparticles from our syntheses exhibited a shallow absorption onset at a wavelength of 750 nm followed by a sharper absorption increase at 600 nm. These qualitatively agree with the band gap range previously reported for bulk and thin film samples of $BaZrS_3$, between 1.75 eV to 1.94 eV.[16,19] However, as noted above, these values fall outside of the desired range for optimal performance in a single-junction solar cell. For ideal power conversion efficiency, theoretical predictions suggest that a band gap of 1.74 eV in $BaZrS_3$ could lead to a maximum efficiency of 28%. To reach the theoretical maximum efficiency of about 33.7%, the Shockley-Queisser limit for single-junction photovoltaic cells, the band gap ideally needs to be further reduced to around 1.34 eV.[38] The introduction of titanium as an alloying element to lower the band gap is one potential approach.

Theoretical insights from Meng *et al*. in a 2016 paper suggested that a titanium-doped $BaZrS_3$ material in an orthorhombic perovskite phase (Figure 1a) could serve as an effective light absorber for thin film solar cells with extremely thin absorber layers.[13] The absorption coefficients of $BaZr_{1-x}Ti_xS_3$ (x = 0.25, 0.5) were predicted to be higher than those of lead halide perovskites, indicating that a considerably thinner chalcogenide perovskite absorber could outperform its halide counterpart in efficiency; however, their results also suggested that these alloys would likely be prone to decomposition into the corresponding ternary phases, and they correspondingly reported unsuccessful attempts to prepare alloys with x = 0.1 and 0.2 through combination of binary sulfide precursors (BaS, TiS_2, and ZrS_2) at 800-1000 °C, which provided only a mixture of the ternary $BaTiS_3$ and $BaZrS_3$ materials.

A synthetic approach relying on sulfurization of $BaZr_xTi_{1-x}O_3$—where solid solutions in the perovskite phase can be prepared throughout the compositional range[39]—has proven more successful in generating $BaZr_{1-x}Ti_xS_3$ alloys, albeit primarily at low levels of titanium incorporation. Reports of these alloys date back at least to 1988 when Okai *et al* attempted to prepare $BaZr_{1-x}Ti_xS_3$ alloys by sulfurization of oxide precursors with CS_2 at 800-1000 °C.[40] They found that the alloy with the composition $Ba(Ti_{0.75}Zr_{0.25})S_3$ uniquely took on a tetragonal perovskite structure when further treated at high pressure and high temperature (1000 °C, 60 kbar), and could be isolated by quenching to room temperature before releasing the pressure. When prepared at normal atmospheric pressure, only mixtures of $BaZrS_3$ and a material with a hexagonal structure of composition $Ba(Ti_{0.75}Zr_{0.25})S_3$ were reportedly formed for x < 0.75, while higher titanium contents led to a $BaZr_{1-x}Ti_xS_3$ ($x \geq$ 0.75) material exhibiting a hexagonal $BaNiO_3$-type structure. Limited experimental data was presented for these compounds and no optical characterization was provided.

More recent studies have focused on the synthesis of properties of $BaZr_{1-x}Ti_xS_3$ alloys that maintain a perovskite phase, as well as the optical characterization of the resulting materials. However, it has generally been found that perovskite-phase $BaZr_{1-x}Ti_xS_3$ materials are only accessible at compositions with $x \leq 0.05$. For example, Nishigaki *et al*. prepared $BaZr_{0.95}Ti_{0.05}S_3$ by sulfurization of a polycrystalline oxide precursor at 1000 °C; the resulting material took on a perovskite *Pnma* structure isostructural to that of unalloyed $BaZrS_3$ with slightly decreased lattice parameters, and with no apparent impurity phases.[19] They reported a band gap of 1.63 eV and an Urbach energy of 70.8 meV for the alloy (compared to 1.95 eV and 28.1 meV, respectively, for $BaZrS_3$), as determined from ellipsometry measurements. Interestingly, the authors were able to prepare the unalloyed $BaZrS_3$ and the chalcogenide alloy $BaZr(Se_{0.4}S_{0.6})_3$ from direct combination of binary precursors at 1000 °C, but noted that this approach was "difficult" for the titanium alloys, necessitating the use of the sulfurization process instead. Furthermore, attempts to prepare an alloy with a higher titanium content (x = 0.1) resulted in phase segregation to produce $BaTiS_3$, similar to the observations of Meng *et al.*[13]

Work by Wei *et al* provided further details about the dependence of the optical and structural properties of $BaZr_{1-x}Ti_xS_3$ alloys on titanium content up to x = 0.04; they used a similar synthetic procedure involving sulfurization of oxide precursors at 1050 °C.[21] Samples with 1, 2, 3, and 4% titanium incorporation showed a systematic, nearly linear decrease in lattice parameter while maintaining an orthorhombic perovskite structure; the measured apparent bandgap also decreased systematically, reaching 1.51 eV with 4% doping. However, titanium concentrations above 5% were observed to compromise the perovskite structure leading to impurity

phases including BaS, TiS_2, ZrS_2 and $BaTiS_3$; no further shift in the crystallographic d-spacing of the alloyed material was observed. While the aforementioned results were all obtained on polycrystalline powders, the preparation of alloyed thin films has also been recently pursued; Sharma *et al*.[22] prepared alloyed oxide precursor thin films by spin-coating and annealing, followed by sulfurization with CS_2 in an attempt to prepare $Ba(Zr_{1-x}Ti_x)S_3$ alloy thin films with a Ti content up to 6%. However, an anomalous and unexplained increase of the apparent crystallographic d-spacing of the alloyed materials relative to unalloyed $BaZrS_3$—opposite of the expected and previously observed results—as well as the presence of large amounts of impurity phases (primarily $BaTiS_3$ and TiO_2) in all samples makes the true composition of these materials unclear.

Overall, these studies have confirmed theoretical predictions that incorporation of Ti^{4+} has a dramatic effect on the bandgap of the $Ba(Zr_{1-x}Ti_x)S_3$ perovskites, even at low levels of alloying. However, work has largely been limited to $x \leq 0.05$, and little characterization of materials with a wider range of Ti^{4+} content is available; notably, recent studies have reported only phase segregation to give hexagonal $BaTiS_3$ for higher values of *x*, rather than the formation of alloyed hexagonal (non-perovskite) phase $Ba(Zr_{1-x}Ti_x)S_3$, although Okai's 1988 paper demonstrated that it is possible to form such a material.[40] Two other limitations of current studies are noteworthy: first, no successful direct synthesis (e.g., from binary and/or monoelemental precursors) of the alloys has yet been reported, only oxide sulfurization requiring temperatures of at least 1000 °C; and second, no unambiguous and clean formation of alloyed thin films has been reported, only polycrystalline powders. Given these limitations, we were interested to investigate whether these alloys could be accessed from solution phase synthesis on a nanocrystal platform, which could open new avenues for synthetic investigation.

In this study, we report the successful synthesis of colloidal nanoparticles composed of Ti-alloyed $BaZrS_3$, $Ba(Zr_{1-x}Ti_x)S_3$, with *x* ranging from 0 to 0.59. The synthesis was achieved using reactive amide precursors in an oleylamine solvent at a temperature of 300 °C; N,N'-diethylthiourea served as the sulfur source, building upon methodologies previously employed in our studies on the synthesis of $BaTiS_3$ and $BaZrS_3$ nanomaterials.[37,41] The $Ba(Zr_{1-x}Ti_x)S_3$ nanomaterials exhibited a phase transition from an orthorhombic distorted perovskite crystal structure (Figure 1A) to a hexagonal non-perovskite phase (Figure 1B) when the measured Ti content reached 15%. This structural transition was concomitant with a morphological evolution, transitioning from the initial $BaZrS_3$ nanoplatelets to nanohexagons, and ultimately, to nanobars. We observed that alloyed nanoparticles in the hexagonal phase with measurable crystallinity begin to form at temperatures as low as 258 °C. As observed in bulk studies, incorporation of Ti^{4+} shifts the apparent absorbance edge and increases the low-energy absorbance of the nanocrystals; at high Ti^{4+} content (in the hexagonal phase) the absorbance in the near-IR increases, consistent with a low bandgap as measured for $BaTiS_3$.[42]

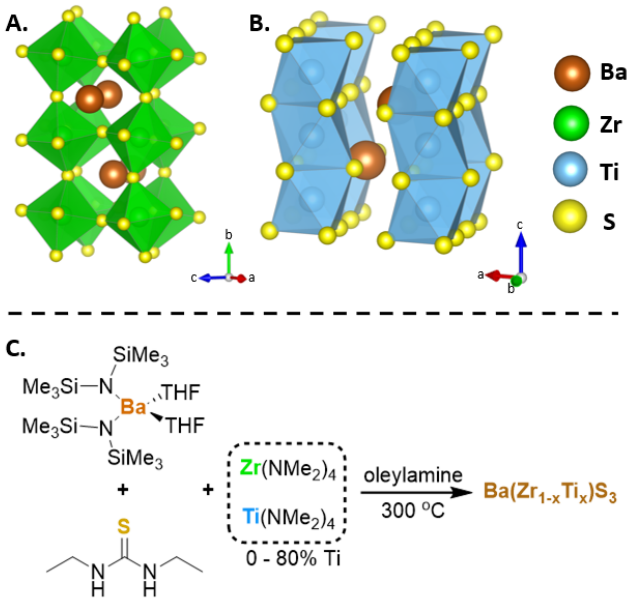

Figure 1. Structural depiction of Ti-alloyed $BaZrS_3$, showcasing (A) the orthorhombic distorted perovskite structure and (B) the non-perovskite hexagonal structure. Panel (C) presents the synthetic scheme employed for the synthesis of titanium-alloyed $BaZrS_3$ nanoparticles.

Methods

Materials and synthetic considerations

General. Tetrakis(dimethylamido)zirconium and -titanium ($Zr[N(CH_3)_2]_4$ and $Ti[N(CH_3)_2]$, 99.8%) were purchased from Sigma-Aldrich and stored in an N_2 glovebox. $Zr[N(CH_3)_2]_4$ was further purified by sublimation before use. N,N'-Diethylthiourea, acquired from Alfa Aesar, was recrystallized from toluene and dried at 60 °C in vacuo overnight. Oleylamine (70%) from Sigma-Aldrich was refluxed at 120 °C over CaH_2, distilled *in vacuo*, transferred to an N_2 glovebox, filtered through activated alumina, and stored over 4 Å molecular sieves. For workups carried out in the glovebox, ethanol was dried by distilling from magnesium ethoxide, and degassed chloroform was dried by passing through activated alumina; both were stored over 4 Å molecular sieves. The barium precursor $Ba[N(SiMe_3)_2]_2(THF)_2$ was synthesized as described by Caulton *et al* with minor modifications as described in our previous work.[41,43]

Synthesis of $Ba(Zr_{1-x}Ti_x)S_3$ nanoparticles. We employed a heat-up approach, adapted from the protocol detailed in our previous research on $BaZrS_3$ nanoparticles.[37,41] In a glovebox, 1.7 g (2.46 mL) of anhydrous oleylamine was used to dissolve 90.8 mg (0.15 mmol) of $Ba[N(TMS)_2]_2[THF]_2$ in a 20 mL vial. This solution was then mixed with 53.8 mg (0.2 mmol) of $Zr[N(CH_3)_2]_4$ in a separate vial. Volumes ranging from 0 µl to 400 µl of a 0.404 M $Ti[N(CH_3)_2]_4$ solution in oleylamine were added to the Ba/Zr precursor solution. This combined mixture was subsequently transferred to a Schlenk tube, which was equipped with a sidearm sealed by a Teflon valve and a Teflon-coated stir bar. Following this, 0.4 g (3 mmol) of solid N,N'-diethyl thiourea was added, and the resulting mixture was stirred for three minutes. Upon removing the flask from the

glovebox, it was connected to an inert gas manifold and subjected to controlled heating at 300°C using a J-KEM PID temperature controller. This temperature was sustained for 30 minutes, after which the system was allowed to return to ambient conditions. For post-reaction procedures, the flask was reintroduced to the glovebox. To isolate the Ti-alloyed $BaZrS_3$ nanocrystals, the crude product was treated with approximately 5 ml each of ethanol and chloroform, followed by vigorous stirring. This mixture was then portioned into two test tubes and subjected to centrifugation at 2800 rpm. The supernatant was discarded, the precipitate underwent a subsequent wash with 5 ml of ethanol, and then it was redispersed in chloroform. The progress of the heat-up reaction was studied by collecting samples at intervals of 5, 10, and 20 minutes during the heating process and subjecting each aliquot to the same work-up procedure. The yield of the reaction was estimated to be approximately 52% (based on the mass of washed, dried nanocrystal precipitate) from a typical sample; however, this should be considered an upper limit of the true yield since the percent contribution of ligands to the sample mass was not explicitly determined.

The sample prepared with 80% nominal Ti^{4+} content used 0.05 mmol of $Zr[N(CH_3)_2]_4$ and 0.2 mmol of $Ti[N(CH_3)_2]_4$, and otherwise followed the standard protocol described above.

Characterization

Powder X-ray diffraction (PXRD). For PXRD measurements, samples were prepared by drop-casting colloidal suspensions onto a zero-background silicon substrate. Data acquisition was conducted using an AXRD Benchtop diffractometer from Proto Manufacturing, employing Cu Kα radiation. This instrument featured a Dectris MYTHEN2 R 1D hybrid photon-counting detector and operated in Bragg-Brentano geometry. Measurements were taken with a step size of 0.020°, employing dwell times ranging from 5 to 15 seconds and a 1 mm collimating slit. A measured background acquired on an empty substrate under the same conditions was subtracted from the data shown. Data refinement was carried out using GSAS-II.[44] Instrument calibration was achieved using a LaB_6 standard.

Transmission electron microscopy (TEM) and energy-dispersive X-ray spectroscopy (EDS) analysis. Samples intended for TEM observation were diluted in chloroform and sonicated. Subsequently, a droplet from this colloidal dispersion was placed on a carbon-coated copper TEM grid and allowed to air-dry. Prior to imaging, samples were stored overnight in a vacuum desiccator. All sample preparations were executed in a glovebox under nitrogen atmosphere. Imaging investigations were carried out using a JEOL 2100 TEM at an operational voltage of 200 kV. Elemental analysis was performed with an Oxford EDS system.

Elemental analysis by inductively coupled plasma mass spectrometry (ICP-MS) analysis. The Ti-alloyed $BaZrS_3$ samples were subjected to two successive washes using 5 ml of chloroform, incorporating sonication and centrifugation steps, to remove residual ligands from the nanocrystals. After washing, nanocrystals were air-dried. Separate portions of each nanocrystal sample were subjected to two different digestion protocols. One portion was treated with an acid mixture of HNO_3, HCl, and HF (in a 3:1:1 ratio) and placed in a hot water bath for 2 hours; analysis of this sample was used to determine the Ti/Zr ratio. The second portion was treated with a 1:1 combination of HNO_3 and HCl acids followed by heating in a hot water bath for 2 hours; analysis of this sample was used to determine the Ba/Zr ratio. After digestion, the acidified samples were diluted to a 100 ml volume using ultrapure deionized water. Analyses were conducted on a Perkin Elmer ELAN DRC II instrument and compared to calibration curves derived from commercial Zr^{4+}, Ti^{4+}, and Ba^{2+} standards.

Safety Note: Hydrofluoric acid (HF) is highly corrosive and toxic. Proper safety measures, including specialized training and appropriate protective gear, are essential when handling HF. Immediate first-aid should be applied if any exposure occurs.[45]

UV–Vis–NIR. Samples intended for absorbance analysis were dispersed in a suitable solvent, either chloroform or tetrachloroethylene, through brief sonication. These samples were subsequently transferred to a quartz cuvette and measurements were conducted using a Perkin Elmer Lambda 900 spectrometer; data from a solvent blank is subtracted from the spectra shown.

Environmental stability tests. To qualitatively evaluate the sample stability under ambient conditions, the colloidal suspension was drop-cast on a zero-background silicon plate intended for PXRD analysis and left exposed to ambient air in the laboratory (average conditions in the laboratory during this period were approximately 20 °C and 40% relative humidity).

X-ray photoelectron spectroscopy. XPS studies were carried out using a PHI VersaProbe II instrument using a monochromated aluminum X-ray source at 1.4866 keV.

Computational methods. Calculations were carried out using the Quantum Espresso suit and the program PWSCF, version 7.2, using the frozen-core projector augmented-wave (PAW) method with the PBESOL functional; further detailed description of the methodology is provided in the Supporting Information.

Results and Discussion

Synthesis

Attempts to prepare multinary compounds present increasingly complex challenges as the number of constituents increases; targeting quaternary $Ba(Zr_xTi_{1-x})S_3$ materials requires balancing the reactivity of up to four different precursors, and finding conditions to favor the formation of the desired phase over

possible binary or ternary phases. We have previously reported the solution-phase syntheses of $BaZrS_3$ and $BaTiS_3$ nanocrystals using metal amide precursors and N,N'-diethylthiourea in oleylamine; given the similar conditions used to access the ternary materials, we felt that it would likely be possible to combine these protocols to prepare alloyed materials. Here, we adapted our prior approach to target $Ba(Zr_xTi_{1-x})S_3$, using a heat-up protocol at a reaction temperature of 300 °C.[37,41] As described in our prior work, the use of highly soluble and reactive metal amide precursors facilitates the formation of the desired sulfide materials, but also necessitates the use of rigorously anhydrous conditions throughout the synthetic procedure; furthermore, the reaction benefits from a high concentration and significant excess of the sulfur precursor.[37,41] Briefly, the reactions were carried out by mixing $Ba[N(TMS)_2]_2(THF)_2$, $Zr[N(CH_3)_2]_4$, N,N'-diethylthiourea, and $Ti[N(CH_3)_2]_4$ in anhydrous oleylamine and then heating the mixture to 300 °C. Under standard conditions, the precursor ratio Ba:Zr:S was maintained at 1:1.3:20, while varying amounts of the titanium amide precursor added (ranging from 0 to 50% of the total B-site cation); for higher titanium contents (80% of total B-site cations), the amount of Zr^{4+} added was concomitantly decreased (see Experimental Section for further details). After 30 minutes, the crude product was cooled to room temperature, and the nanocrystals were washed with anhydrous ethanol and chloroform. It was observed that the resulting nanocrystals could be suspended in chloroform with sonication to form a well-dispersed colloid. In discussions below, the percentage of titanium precursor introduced relative to the total B-site cation precursor content in the reaction mixture is referred to as the "nominal" titanium content, while the actual titanium content of the isolated samples was measured by ICP-MS; unless otherwise stated, all Ti^{4+} amounts (reported as x in $Ba(Zr_xTi_{1-x})S_3$) referred to in the discussion and figures below are the measured amounts.

Power X-ray diffraction and structural characteristics

As noted in the introduction, $BaZrS_3$ crystallizes in a distorted orthorhombic perovskite structure ($GdFeO_3$-type, *Pnma*) while $BaTiS_3$ takes on a non-perovskite hexagonal structure ($BaNiO_3$-type, $P6_3/mmc$) characterized by one-dimensional chains of face-sharing TiS_6 octahedra. The inability of $BaTiS_3$ to form a stable perovskite is likely related to the small size of the Ti^{4+} ion, which results in its octahedral factor ($\mu = r_{Ti}/r_S$) being outside of the optimal range for perovskite formation.[14] Therefore, if a $Ba(Zr_{1-x}Ti_x)S_3$ alloy is accessible for all values of x, it is expected that a phase change from orthorhombic to hexagonal will occur at some point along the compositional range. Indeed, Okai *et al.* reported that for $x \geq 0.75$, bulk polycrystalline $Ba(Zr_{1-x}Ti_x)S_3$ takes on a $BaNiO_3$ structure type; however, intermediate compositions with $x \leq 0.75$ gave rise to mixtures in their report.[40]

Nanocrystals of unalloyed $BaZrS_3$ and $BaTiS_3$ have both been characterized by powder X-ray diffraction (PXRD) in prior work, and a few key observations about the structure and diffraction properties of the particles are reiterated here for context.[41,46,47] In the case of $BaZrS_3$, it was observed that the nanocrystals (depending on the reaction conditions) exhibited powder X-ray diffraction characteristics that were not completely consistent with the reported bulk *Pnma* structure, although analysis by X-ray total scattering and pair-distribution function (PDF) analysis suggested that the local structure was still perovskite-like.[46,47] The exact nature of the structural distortion that seems to occur on the nanoscale is not currently precisely known, due to the difficulty of structure determination on the nanoscale. Here, we use the *Pnma* structure (as reported by Lelieveld *et al*)[48] as an approximation for the $BaZrS_3$ and alloyed perovskite nanocrystals, while recognizing that this introduces some uncertainty in the structural analysis (Figure 2). In the case of $BaTiS_3$, it is known from the bulk literature that this material is in most cases better described as $BaTiS_y$ ($y \leq 3$) and is characterized by an incommensurate composite structure whose structural parameters and diffraction pattern depend strongly on the sulfur substoichiometry. In the nanocrystals, this stoichiometry depends on the reaction conditions (including time and concentration) and is difficult to precisely control in practice. Typical values of y for the nanocrystals are approximately ~2.7 and above. This results in sample-to-sample

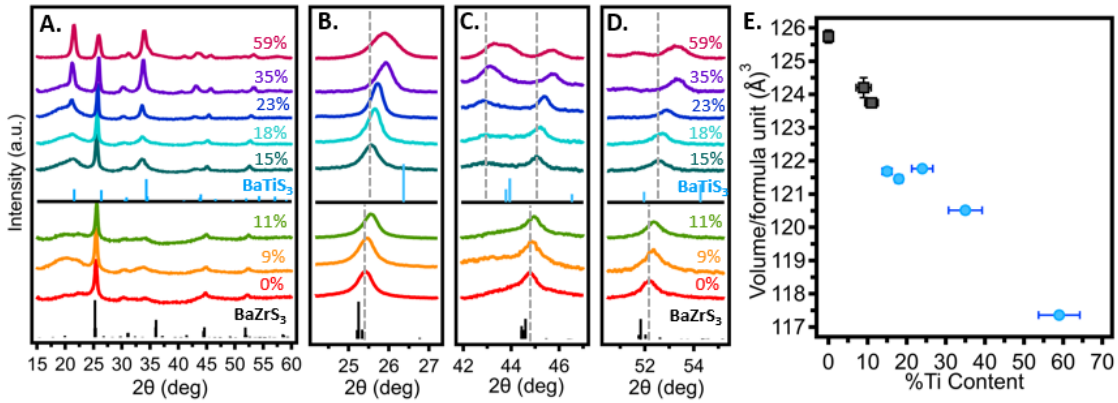

Figure 2. Structural analysis of Ti-alloyed $Ba(Zr_{1-x}Ti_x)S_3$ nanocrystals and variation in unit cell volume as a function titanium content. (A) PXRD data for $Ba(Zr_{1-x}Ti_x)S_3$ nanocrystals with different percentage contents of Ti^{4+}, compared to the reference structure reported for $BaZrS_3$ in orthorhombic distorted perovskite (*Pnma*) and $BaTiS_3$ in hexagonal phase ($P6_3/mmc$). Note that the broad feature around 20° in most samples corresponds to scattering from amorphous components of the sample including excess ligands.[35,36] (B-D) Magnified views of the PXRD data. Vertical dotted lines are guides to the eye to help visualize peak shifts. (E) Volume per formula unit, derived from LeBail fitting of the PXRD data, as a function of measured titanium content (ICP-MS).

variation of the structural parameters, which are most apparent in the length of the apparent crystallographic *c* unit cell axis; changes in the length of the *a* axis are much smaller but trend in the opposite direction from *c*.[47,49]

In Figure 2, the results of the powder X-ray diffraction analysis for $Ba(Zr_{1-x}Ti_x)S_3$ nanocrystals with different titanium alloying levels are presented, along with the volume per formula unit plotted against the titanium content measured using ICP-MS. The unit cell parameters were extracted from the PXRD data using LeBail refinement (see Supporting Information for details, Table S1 and Figures S3-S10); because of the change in space group, plotting the volume per formula unit provides a clearer picture of the alloying across the compositional range than the individual lattice parameters, and confirms a systematic decrease in volume as the smaller Ti^{4+} ions are incorporated across both phases. This trend is suggestive of successful alloying rather than the presence of mixtures of discrete $BaTiS_3$ and/or $BaZrS_3$ phases. As shown in Figure 2a, the X-ray diffraction patterns obtained for $Ba(Zr_{1-x}Ti_x)S_3$ nanocrystals with low levels of titanium alloying (x = 0, 0.09, 0.11) are qualitatively similar to those previously reported for unalloyed $BaZrS_3$ nanocrystals, which were assigned to a distorted perovskite structure.[28] LeBail refinement of the unit cell parameters (*Pnma*) and unit cell volume showed a small but systematic decrease in these parameters as Ti^{4+} content increased from 0 to 11%. We attempted to fit the 11% alloy PXRD data to a hexagonal $BaNiO_3$ structure type as an alternative, but this consistently gave rise to higher R-values and implausible lattice parameters (e.g. *c* = 4.9 *vs*. the measured *c* = 5.9 for hexagonal $BaTiS_3$, see Figure S5). Therefore, we conclude that nanocrystals with a measured Ti^{4+} content of up to 11% are structural analogues of the unalloyed perovskite $BaZrS_3$. However, we note as a caveat that, given the limitations of the data, it is difficult to rule out that some samples could be a mixture of phases, e.g. with a portion of a hexagonal-phase alloy as a minor component

In contrast, for $Ba(Zr_{1-x}Ti_x)S_3$ with 15% titanium alloying and higher, the diffraction peaks are more consistent with the predicted pattern of $BaTiS_3$ with the $BaNiO_3$ structural type (*P6₃/mmc*),[50,51] as depicted in Figure 2a. Notably, as the titanium doping level increases past 11%, new diffraction peaks emerge at 21.5° and 34.3°, associated with the (101) and (201) planes in the $BaNiO_3$ structure type (see Figure S2 for labeled peaks). A magnified view in Figure 2B-D of the PXRD pattern in the regions of three characteristic peaks reveal a generally systematic shift of three diffraction peaks towards higher angles with increasing titanium content; the peak positions tend towards but do not yet reach the expected positions for unalloyed $BaTiS_3$. The analysis of the *d*-spacing and unit cell parameters as they relate to titanium content is complicated by the fact that, as discussed above, sample-to-sample variation in the lattice cell parameters is expected due to small variations in the sulfur stoichiometry, which may account for deviations from the expected trend in some instances. This is consistent with the fact that the fitted value of the *c* lattice parameter (which is more strongly affected by these variations) does not cleanly vary systematically with *x*, while the values of *a* and the volume per formula unit both show a generally decreasing trend (Figure 2E and Figure S11). Despite this complication, the overall trend, especially as it relates to the decrease in volume per formula unit as the Ti^{4+} content increases, is clear and remains consistent with successful alloying.

Compositional Analysis

The standard reaction conditions for our nanocrystal synthesis involve a slight excess of the B-site metal cations (Zr^{4+} and Ti^{4+}); since excess B-site cations are removed during the washing process, the Ti^{4+} content in the isolated samples does not necessarily correspond exactly to the nominal amount added to the reaction mixture. The actual elemental compositions of the Ti-alloyed $Ba(Zr_{1-x}Ti_x)S_3$ samples were determined by ICP-MS (Figure 3). As the amount of titanium precursor added to the reaction mixture was increased, a corresponding systematic increase in the measured Ti^{4+} content is observed. Throughout most of the range, the measured Ti^{4+} content is slightly lower than the nominal content (e.g. 80% nominal Ti^{4+} led to 59% measured Ti^{4+}), suggesting that there may be slight preference for Zr^{4+} incorporation under our reaction conditions, perhaps due to differing reactivities of the metal precursors or other kinetic or thermodynamic factors related to the growth process. The Ba^{2+} content was also measured by ICP-MS and the Ba:(Zr+Ti) ratios of the $Ba(Zr_{1-x}Ti_x)S_3$ samples are close to the expected stoichiometry. For example, for x = 0, x = 0.09, and *x* = 0.11, the ratios stand at 1:1.05, 1:1.0, and 1:1.2, respectively (see Table S2). On average, the B-site cations (Zr and Ti) were observed by ICP-MS quantification to be slightly in excess relative to Ba. It is not uncommon for the overall stoichiometry of small nanocrystals, which are characterized by a high surface-to-volume ratio, to deviate from the theoretical bulk stoichiometry due to surface termination; however, it is difficult to rule out that the apparent excess Zr and Ti could be due the presence of small amounts of amorphous Ti- and Zr-containing impurities such as oxides, or due to challenges in completely digesting the samples for ICP analysis.[52,53] To attempt to address this uncertainty, and to gain a more microscopic view of the elemental composition, energy dispersive X-ray spectroscopy

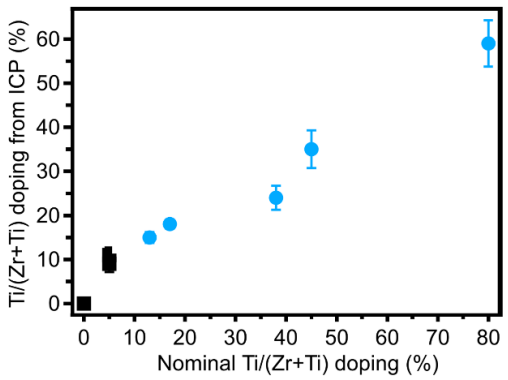

Figure 3. Variation of measured Ti^{4+} content as a function of the nominal titanium content. The black closed squares correspond to samples assigned to the orthorhombic perovskite phase and the blue closed circles correspond to samples in the hexagonal $BaNiO_3$ phase.

(EDX) measurements coupled with TEM imaging were also carried out.

Figures 4 shows the EDX elemental maps for representative $Ba(Zr_{1-x}Ti_x)S_3$ samples with x = 0 and x = 0.59 (see below for further TEM imaging of these particles; EDX maps for other samples are provided in Figures S12-S13). The elemental mapping reveals a uniform distribution of these elements throughout the doped nanocrystals, indicative of a generally homogeneous composition; the uniform distribution of sulfur co-occurring with the metal ions also suggests that contamination with discrete oxide phases, if any, is relatively minor. The EDX analysis of alloyed samples for the cases with x = 0 and x = 0.59 revealed percentage compositions of Ba:Zr:Ti:S as 27:19:0:55 and 29:9:11:51, respectively (Table S15). The EDX measurements suggest an excess of barium compared to the total B-site cations (Zr+Ti); this contrasts with the slightly barium-deficient composition measured by ICP-MS. The precise cause of this discrepancy has not yet been investigated in detail, but could be linked to variations in sample preparation methods between the two elemental analysis techniques (EDX and ICP). It should also be noted that the measured EDX compositions of titanium and barium may be susceptible to inaccuracies due to significant overlap of the Ba and Ti characteristic X-ray lines.

Evolution of nanoparticle size and morphology

The morphology of unalloyed $BaZrS_3$ nanocrystals and the alloyed $Ba(Zr_{1-x}Ti_x)S_3$ samples, prepared under standard conditions, was evaluated using transmission electron microscopy (TEM) imaging. Figures 5a-h present TEM images of $Ba(Zr_{1-x}Ti_x)S_3$ samples with values of *x* ranging from 0 to 0.59. Notably, the sample's morphology transforms from nanoplatelets to nanohexagons and ultimately to nanobars. Specifically, samples synthesized with low titanium doping levels (*x* = 0 to 0.15) exhibit nanoplatelet structures (Figures 5a to 5d). At 18% Ti content, the nanocrystals show a more agglomerated morphology resembling nanoflowers; beyond that (23% Ti), a clear hexagonal morphology begins to take shape (Figures 5e-f). The sample with 35% titanium doping is characterized by relatively large and well-defined hexagonal particles. (Figure 5g). Samples with intermediate compositions (e.g. 44% Ti content, see below) showed a mixture of nanobar and nanohexagon morphologies. The alterations in nanocrystal morphology are correlated with the observed phase change, and in particular with the emergence of the hexagonal structure at higher titanium content. The presence of lattice fringes, clearly visible in Figure 5g, confirms the high crystallinity of the alloyed nanohexagons. Figure 5i shows the average sizes of the imaged particles as a function of the measured titanium content. At low doping levels (*x* = 0 to 0.11), the average width of the perovskite-phase nanoplatelets does not change significantly, ranging from 16 ± 4 nm to 18 ± 5 nm. However, during the transition to the hexagonal phase for doping levels of *x* = 0.15 to 0.35, the average size appears to steadily increase as the nanocrystals take on a more well-defined hexagonal shape, ranging from 24 ± 5 nm to 43 ± 10 nm. For the nanobar particles at higher titanium content, a slight decrease in overall size is observed concomitant with the change in morphology. The observed trends in morphology, especially in the limits of high- and low-titanium content, are consistent with what we have previously reported for $BaZrS_3$ and $BaTiS_3$ nanoparticles—specifically, previously reported $BaZrS_3$ nanoparticles have a rather poorly-defined, aggregated nanoplatelet morphology (Figure 5a) while $BaTiS_3$ nanoparticles tended to have an elongated nanorod morphology, although this was dependent on the reaction conditions.[37,41] Interestingly, well-defined and highly crystalline nanohexagon-like particles of the type observed for $BaTi_{0.35}Zr_{0.65}S_3$ were not observed in the case of unalloyed $BaTiS_3$ under any of the reaction conditions we previously studied.

Figure 6a shows a transmission electron microscopy (TEM) image of $Ba(Zr_{1-x}Ti_x)S_3$ nanoparticles for *x* = 0.35, showcasing lattice fringes, and the fast Fourier transform (FFT) of the image (inset). The analysis of the d-spacing from line profiles of the highlighted regions of the particle (Figure S15) yields values of 0.34 nm and 0.59 nm, which could correspond to the $(1\bar{1}0)$ and $(2\bar{1}0)$ sets of diffraction planes. Additionally, electron diffraction was conducted on a representative $Ba(Zr_{1-x}Ti_x)S_3$ sample (*x* = 0.28), which confirmed the crystallinity of the

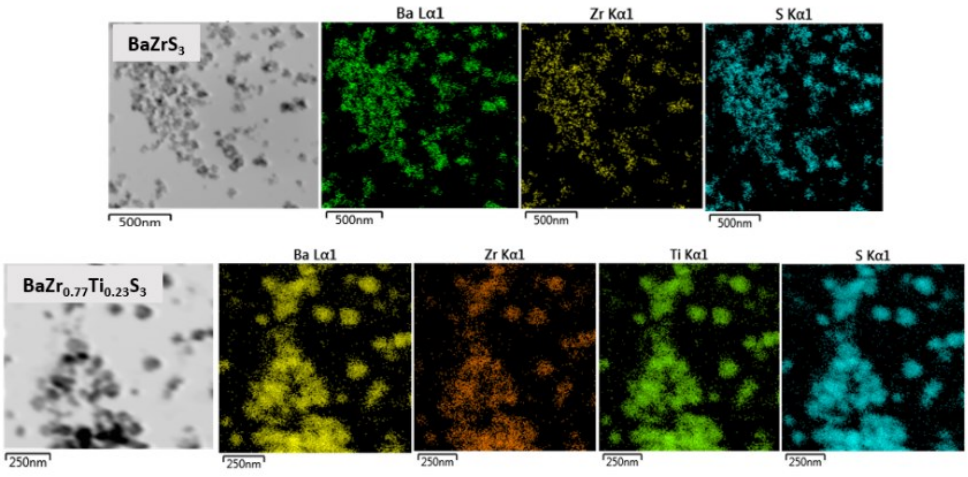

Figure 4. EDX mapping of Ti-alloyed $Ba(Zr_{1-x}Ti_x)S_3$ with (top) x = 0 and (bottom) x = 0.23.

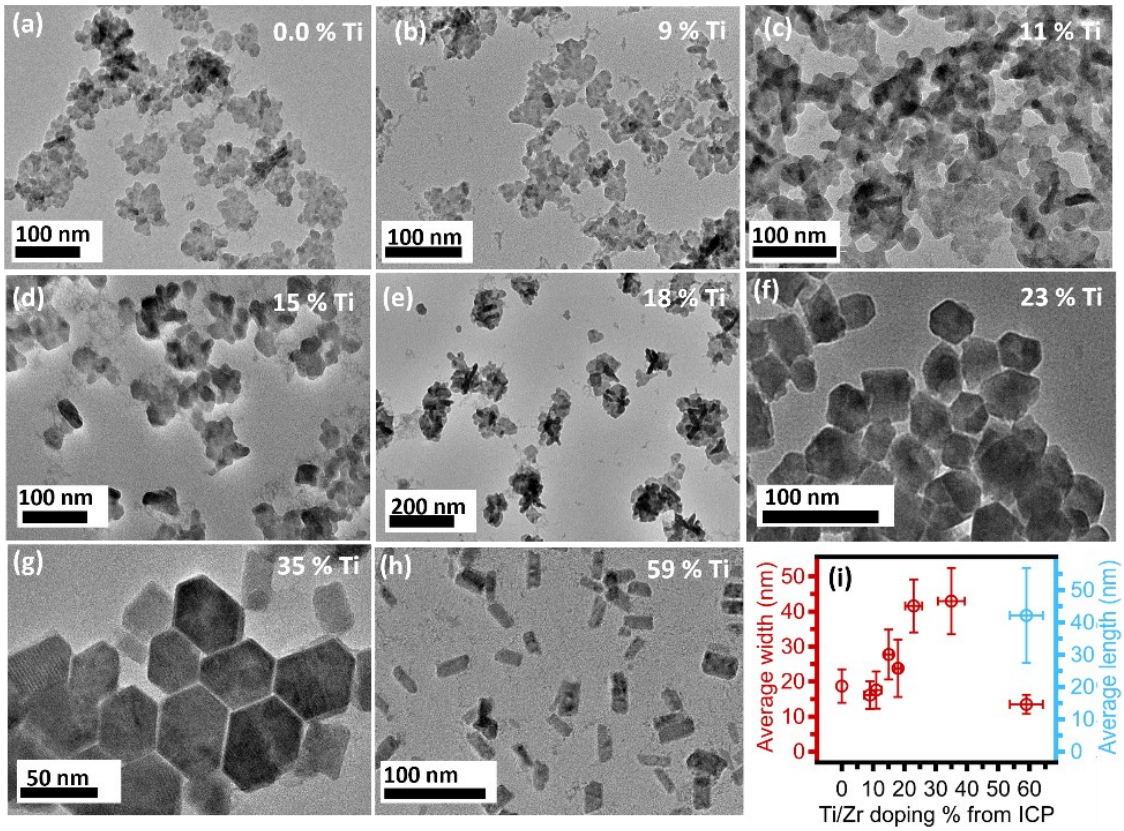

Figure 5. Morphological evolution of Ti-alloyed $Ba(Zr_{1-x}Ti_x)S_3$ viewed using TEM. TEM image of Ti-alloyed $Ba(Zr_{1-x}Ti_x)S_3$ (a) x = 0 (b) x = 0.09 (c) x = 0.11 (d) x = 0.15. (e) x = 0.18 (f) x = 0.23 (g) x = 0.35 (h) x = 0.59 (i) Average size distribution of the Ti-alloyed $Ba(Zr_{1-x}Ti_x)S_3$ nanoparticles.

imaged particles and was consistent with the diffraction pattern observed by PXRD (Figure S14).

Optical properties

The optical band gap of bulk $BaZrS_3$ has been reported in a range of 1.75 to 1.95 eV by different sources; Sopiha *et al.* have suggested that this variation is likely due to a combination of factors potentially including (Urbach) band tailing, the presence of forbidden or partially forbidden transitions at the band gap, and/or the presence of small amounts of impurity phases with lower bandgaps.[12–14,16–22,46,54] A blue-shifted bandgap of around ~2.3 eV was estimated in a previously report of $BaZrS_3$ nanocrystals by Tauc-type analysis of the optical spectrum, with complementary photoluminescence at 2.08 eV, suggesting the possibility of quantum confinements effects.[54] As discussed above, alloying with Ti^{4+}, even at relatively low levels, has been predicted computationally and demonstrated experimentally to have a strong effect on the absorbance spectrum and bandgap, increasing the absorbance at low-energies and lowering the bandgap to the range of 1.51-1.63 eV for 4-5% Ti doping. However, the absorbance spectra for samples at higher Ti^{4+} alloying levels, including past the phase transition to hexagonal, have not been previously discussed. In general, the pseudo-one dimensional hexagonal-phase ABS_3 compounds have significantly lower bandgaps—for $BaTiS_3$ the bandgap lies near 0.3 eV, while the computationally predicted band gap for the hypothetical hexagonal-phase $BaZrS_3$ is approximately 0.4 eV.[15] Nanocrystals of $BaTiS_3$ were observed to have absorbance throughout the NIR region, as expected based on the material's low bandgap, and to exhibit strong absorbance peaks at 1.55 eV and near 0.8 eV.[41]

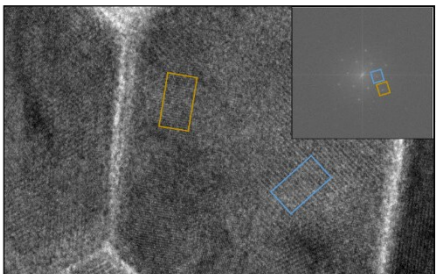

Figure 6. TEM image of $Ba(Zr_{1-x}Ti_x)S_3$ nanoparticles with x = 0.35, highlighting regions where lattice fringes are visible. The inset shows the FFT of the TEM image, with spots corresponding to the lattice spacing observed in the highlighted regions indicated.

UV-Vis-NIR extinction spectra of the $Ba(Zr_{1-x}Ti_x)S_3$ nanocrystals as colloids in chloroform are shown in Figure 7, separated into the orthorhombic-phase samples at low x (Figure 7a) and the hexagonal-phase samples at high x (Figure 7b); photographs of the samples are given in Figure S16, showing a gradual change in color from dark brown-red to brown-black. The data are normalized at 500 nm (2.48 eV) to facilitate comparison between different samples. At low titanium content, the perovskite-phase samples show similar sloping absorption spectra (Figure 7a), but the proportion of lower-energy absorption increases as the titanium content increases, and the apparent absorption onset shifts to lower energy. The effect is qualitatively similar to that reported by Wei *et al.* for doping contents of 1-4%.

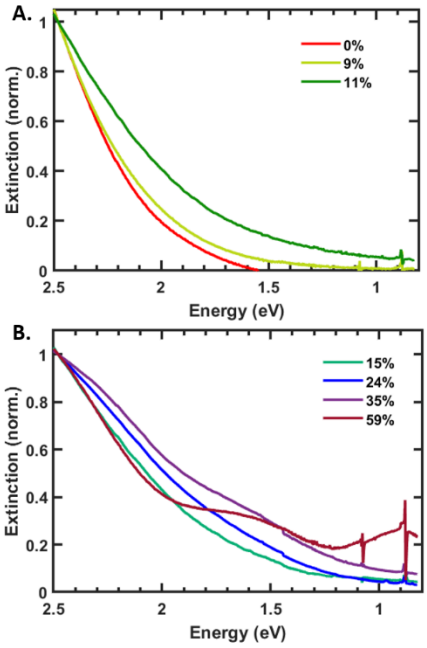

Figure 7. UV-vis extinction spectra of $Ba(Zr_{1-x}Ti_x)S_3$ nanoparticles, acquired in chloroform. (A) Spectra $BaZr_{1-x}Ti_xS_3$ nanocrystals where x = 0 to 0.11, where nanocrystals maintain an orthorhombic perovskite structure. (B) Spectra for hexagonal-phase nanocrystals with x = 0.15 to 0.59. Sharp features around 0.9-1.2 eV are background from the solvent.

As the nanocrystals transition to a primarily hexagonal phase at $x \geq 0.15$, the low-energy absorbance continues to increase and tail into the near-IR. At x = 0.35 and x = 0.59, features more clearly reminiscent of the $BaTiS_3$ nanocrystal spectra appear, including a peak at 1.55 eV, at essentially the same energy that it appears in the unalloyed $BaTiS_3$ particles. Only at 59% Ti content does the strong near-IR peak previously observed for $BaTiS_3$ nanorods become apparent, here at an energy of 0.93 eV; this energy lies at the upper end of the range over which this peak was observed for the unalloyed particles.[41]

Effect of reaction time and temperature

To further probe the formation of $Ba(Zr_{1-x}Ti_x)S_3$, we explored the influence of temperature and time on the morphology and composition of the particles. Using the standard heat-up reaction conditions, we collected three samples at reaction times of 10, 20, and 30 minutes, starting as the temperature increased from room temperature to 300°C. The initial 10-minute sample was obtained while the temperature was still rising, at 258°C; the 20-minute and 30-minute samples were taken after the sample reached the final reaction temperature of 300°C.

As shown in Figures 8a-c, TEM images reveal a combination of nanoscale hexagons and bars that form within the first 10 minutes of the reaction, with little change in the size and shape of the particles (Figure 8d) over the course of the reaction up through the 30-minute sample. Higher resolution images reveal that well-defined lattice fringes are visible even in the 10 minute-sample, suggesting that highly crystalline particles have already formed (Figure S17). ICP-MS analysis indicated a consistent titanium content of approximately x = 0.44 ± 0.1 in

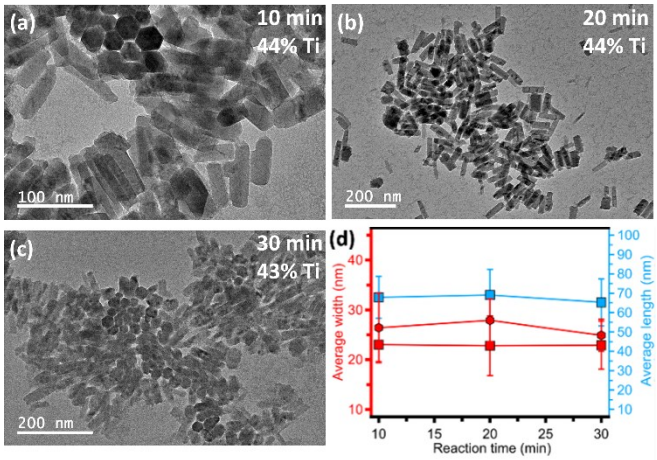

Figure 8. TEM images of $Ba(Zr_{1-x}Ti_x)S_3$ nanocrystals from reaction aliquots taken at (a) 10 minutes at 258 °C (b) 20 minutes at 300 °C (c) 30 minutes at 300 °C. (d) Average size distribution of nanocrystals at each time point.

all three samples, suggesting that there are no further significant changes in the metal ion composition after initial formation of the particles. We also tested longer reaction times (1 hour) for several different Ti^{4+} concentrations, which did not seem to noticeably change the outcome of the reaction in terms of the particle size and composition as measured by PXRD, but did result in an increased tendency to form crystalline impurities (Figure S18).

Figure 9 shows the PXRD data for the three samples taken between 10 to 30 min. An aliquot collected earlier, at 5 minutes of reaction time when the temperature had reached approximately 200 °C, did not exhibit observable crystallinity according to PXRD. However, the diffraction patterns of samples collected at 10 minutes (258 °C) and later at the final reaction temperature (300 °C) were consistent with nanocrystals with the hexagonal $P6_3/mmc$ structure. Slight changes in the diffraction pattern during the course of the reaction mirror what was previously observed in our study of the reaction-time-dependent properties of unalloyed $BaTiS_3$ nanorods.[41] Small shifts in the positions of certain diffraction peaks are evident when comparing samples taken at 20 and 30 minutes to those from the shorter 10-minute reaction at 258°C (Figure 9). Specifically, diffraction peaks corresponding to the (101), (002), and (201) planes exhibit a shift towards higher angles as the reaction progresses and reaches higher

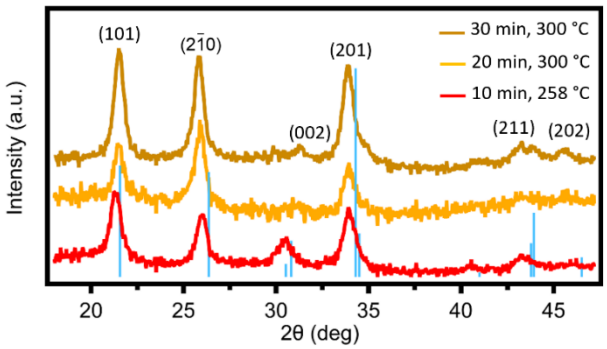

Figure 9. PXRD data of $Ba(Zr_{1-x}Ti_x)S_3$ aliquot reaction taken at different times during the course of heating from room temperature to 300 °C. The blue lines correspond to a reference pattern calculated for unalloyed $BaTiS_3$.

temperature. Similar changes have been observed in the solid state; in a study by Saeki et al.,[49] it was observed that raising the reaction temperature from 750 °C to 900 °C caused increased sulfur deficiencies ($BaTiS_{2.7}$–$BaTiS_{9.3}$), which resulted in an apparent shortening in the apparent *c*-axis periodicity of the structure.

Stability

The superior stability of $BaZrS_3$ under ambient conditions is generally cited as one of its most significant potential advantages relative to the lead halide perovskites, and studies on bulk powders suggest that this stability also extends in part to alloyed $Ba(Zr_{1-x}Ti_x)S_3$ materials. For a Ti-alloyed $Ba(Zr_{1-x}Ti_x)S_3$ bulk powder prepared with 4% titanium, Wei *et al.* reported that minimal degradation was observed after one hour of annealing under O_2 at 500 °C, or after 890 hours at room temperature under ambient atmosphere, similar to their results for unalloyed $BaZrS_3$; however, upon raising the annealing temperature to 800 °C, significantly more degradation was observed for the alloyed sample than for $BaZrS_3$ itself, although the latter also showed partial degradation.[21] This suggested that the stability of the alloyed material was somewhat compromised even at low levels of titanium incorporation. Therefore, we were interested to test whether a similar effect could be observed in nanocrystals, where atmospheric degradation is often accelerated due to the high surface-to-volume ratio of the particles.

To assess the stability of low and high titanium-alloyed $Ba(Zr_{1-x}Ti_x)S_3$ nanocrystals, specifically with x values of 0.11 and 0.35, we exposed these two samples to ambient conditions and monitored them using PXRD over a span of 4 to 8 weeks (Figure 10A-B). In the case of the nanocrystals with 11% titanium alloying, the PXRD data reveals a gradual broadening of peak widths, indicative of partial crystallinity loss, likely due to surface oxidation upon exposure to air. Furthermore, an unidentified peak emerged after 8 weeks, suggesting a possible formation of secondary phases; however, some amount of nanocrystalline $Ba(Zr_{1-x}Ti_x)S_3$ is still detectable at the end of this time (Figure 10A). The alloyed hexagonal-phase $BaZr_{0.65}Ti_{0.35}S_3$ nanocrystals (Figure 10B) showed poor stability under ambient conditions, with no detectable crystalline material remaining after 4 weeks.

Interestingly, this outcome differs from our previously reported stability findings for unalloyed $BaZrS_3$ and $BaTiS_3$ under similar conditions.[47] The unalloyed $BaZrS_3$ showed little to no discernible degradation after 9 weeks in air, compared to significant (albeit incomplete) degradation for the perovskite-phase 11% Ti-doped sample. While unalloyed hexagonal-phase $BaTiS_3$ did show some loss of crystallinity over a similar time period, attributed to surface oxidation, the majority of the sample appeared to persist in the $BaTiS_3$ phase, in contrast to the complete degradation observed here for the hexagonal-phase 35% Ti-containing sample.[41] A close examination of the PXRD data for the 11%-doped sample during the stability study shows a slight shift of the position for the prominent peak near 25.5° over time; in particular, the peak shifts to lower angles

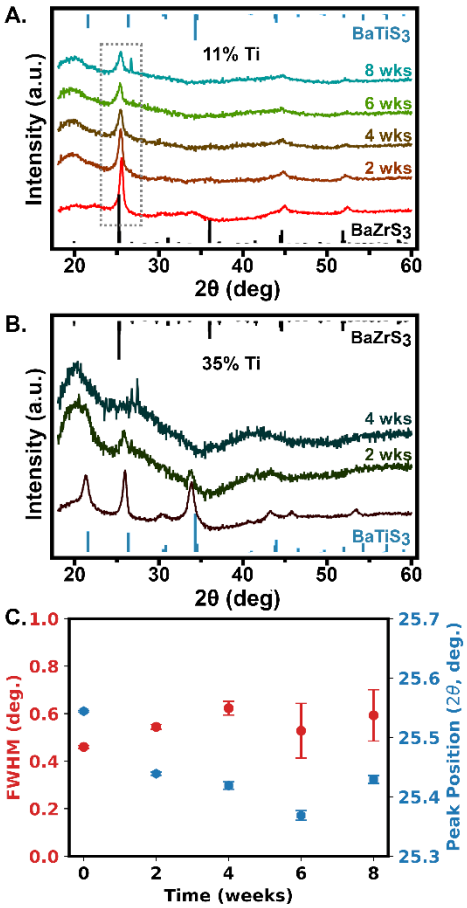

Figure 10. Investigations of the environmental stability of nanocrystals in the $Ba(Zr_{1-x}Ti_x)S_3$ system. Panels (A) and (B) show PXRD patterns for nanocrystals with $x = 0.11$ (A) and $x = 0.35$ (B) upon exposure to ambient atmosphere for up to 8 weeks. The black and blue sticks in (A) and (B) correspond to the calculated reference patterns for $BaZrS_3$ and $BaTiS_3$, respectively. In panel (C), the peak position and peak FWHM are tracked over time for the 11% Ti sample shown in panel (A).

over the first six weeks. This would be consistent with a decrease of the titanium content in the nanocrystalline components of the material, perhaps due either to ion migration and extrusion of titanium to the surfaces of the particles, or preferential degradation/amorphization of more titanium-rich areas. The reason for the apparent peak shift back towards higher angles at week 8 is unclear, but perhaps could be related to increasing incorporation of oxygen especially near the surface.

Computational comparison of orthorhombic and hexagonal $Ba(Zr_{1-x}Ti_x)S_3$ phases

Several prior works have used DFT computations to predict the electronic structure and optical properties of $BaZr_{3-x}Ti_xS_3$ alloys; in addition to the original report by Meng *et al.* discussed above, computational work was presented alongside experimental work by Nishigaki *et al*. and Sharma *et al.*; further computational studies were also reported recently by Kanoun *et al.*, including numerical simulations of solar device performance.[13,19,22,24] Computations on the related material $BaHf_{3-x}Ti_xS_3$ by Kong *et al.* also gave rise to similar results about the impact of Ti^{4+} doping on the perovskite.[55] Despite differences in methodology and small differences in the

quantitative results, these DFT studies have had qualitatively similar outcomes, showing a steep drop in band gap upon the incorporation of even low levels of titanium, as described further below. However, previous computational work has assumed that an orthorhombic perovskite phase is maintained throughout the compositional range, inconsistent with experiment, and has not examined other details such as the effect of the distribution of Ti^{4+} ions on the electronic structure. We were interested in carrying out DFT calculations on both the orthorhombic and hexagonal phases to further contextualize our results about the phase preferences of the alloy system and to probe the impact of dopant distribution.

The structures of $BaZrS_3$, $BaTiS_3$, and $BaZr_{1-x}Ti_xS_3$ for Ti^{4+} contents of 6.25%, 12.5%, 25%, and 50% were optimized in both the orthorhombic and hexagonal phases using the reported *Pnma* and *P6$_3$/mmc* crystal structures, respectively, as the starting points. A 2x1x2 supercell was used for the orthorhombic phase and a 2x2x2 supercell for the hexagonal phase, resulting in 16 independent B-site cations in both cases; for alloyed structures, 1, 2, 4, or 8 of the zirconium ions in the B-sites were replaced by titanium. In the cases with more than one Ti^{4+} atom, multiple possible structures with different arrangements of the dopant ions were considered. The possible structures were generated with the program Supercell and a subset of structures were selected for optimization, specifically including structures with clustered Ti^{4+} ions, well-separated and ordered Ti^{4+} ions, and some with a more random distribution.[56] Computational parameters (see Supporting Information) were selected to give good agreement with the experimentally observed crystal structure of $BaZrS_3$ and to converge the calculated energies at reasonable computational cost given the large systems involved.

A comparison of the calculated enthalpy of the orthorhombic and hexagonal phases at each composition is shown in Figure 11a, where the enthalpy relative to the most stable calculated orthorhombic structure is shown; enthalpies are given per mole of the formula unit. Consistent with experiment, the orthorhombic perovskite phase is favored for the pure $BaZrS_3$ material, while the hexagonal pseudo-one-dimensional phase is favored for the pure $BaTiS_3$ material. There is a nearly linear decrease in the relative energy of the hexagonal $BaZr_{1-x}Ti_xS_3$ from x = 0 to x = 1, with a predicted inversion near 70% Ti. The calculation, therefore, does overestimate the stability of the orthorhombic perovskite phase for intermediate alloyed compositions, given that we observed experimentally a change in phase to hexagonal in the range of 11-15% Ti. Nevertheless, the general trends are consistent experimentally and computationally. There are several possible factors that may contribute to the imperfect agreement, including the fact that the calculations do not capture the true nature of the hexagonal structure as an incommensurate composite lattice,[49] possible differences between nanoscale materials and bulk, the fact that our reactions may occur at least in part under kinetic control rather than being fully thermodynamically controlled, and practical limitations to the accuracy of the DFT calculations. Calculations of the volume per formula unit follow the same trend as those observed experimentally (Figure 11b). Interestingly, in all cases where multiple possible distributions of the alloyed ions were tested, the lowest energy relaxed structure was a relatively high-symmetry structure with the minority ions distributed homogeneously, without any nearest-neighbor pairs, rather than clustered; for the 50% Ti case the lowest-energy structure was characterized by precisely alternating Zr and Ti ions. The low-energy structures and selected alternate structures are shown below (12.5% Ti, *vide infra*) and in the SI (25% and 50% Ti, Figures S21-S22).

Calculations of the electronic structure using GGA+U methods gave an estimate of the band gap for $BaZrS_3$ in the orthorhombic perovskite phase of 1.64 eV. As is common with DFT-GGA methods, this somewhat underestimates the experimentally determined values which have ranged from ~1.74 eV to 1.94 eV, and is slightly below the value of 1.76 eV determined from calculations at the HSE06 level. However, because of the large size of the systems used for calculating the alloyed systems especially at low Ti^{4+} content, HSE06 calculations were considered impractical, and the GGA+U methods can reproduce well the trends in the bandgaps as well as the density-of-states and band structures despite the underestimation of the absolute value, as confirmed by prior computational work on chalcogenide perovskite systems.[13] Results in the orthorhombic perovskite phase are generally consistent with those previously reported, marked by a steady decrease in bandgap as Ti^{4+} is incorporated into the lattice. We noted an initial particularly sharp drop in the bandgap upon incorporation of the first Ti^{4+} ion into the calculated system (6.25% doping, Figure 11c); after that, the bandgap continues to decrease as more Ti^{4+} is incorporated, albeit more gradually.

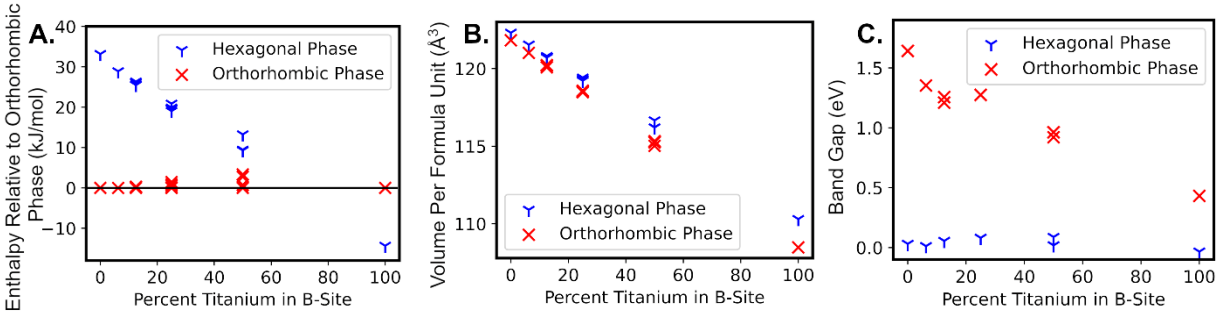

Figure 11. Computationally determined dependence of enthalpy (A), volume per formula unit (B), bandgap (C), and band edge energies (D) on the percent of titanium ions in the B sites. Enthalpy is given per formula unit and relative to the lowest energy calculated structure for a given composition.

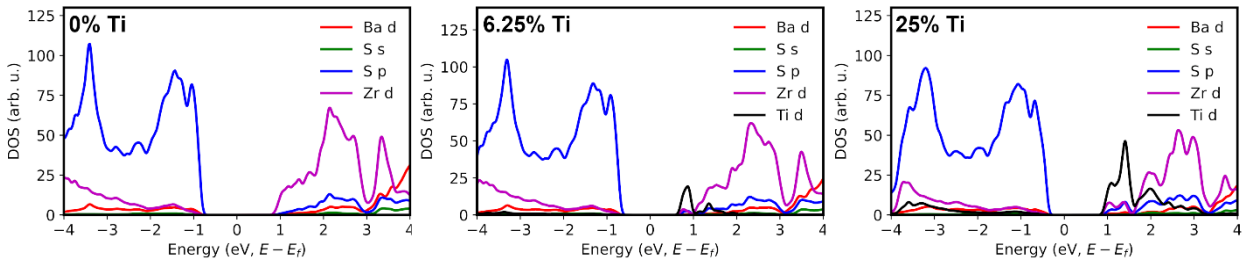

Figure 12. Plots of the calculated partial density of states for selected atomic orbitals for $Ba(Zr_{1-x}Ti_x)S_3$ in the orthorhombic perovskite phase for different percentage Ti contents. Energies are plotted relative to the Fermi level (E_f), which is set to the middle of the bandgap.

An examination of the partial density of state (PDOS) plots for some of these compositions helps contextualize these results (Figure 12 and Figures S19-S20). In these materials, the valence band edge is composed largely of sulfur p-states while the conduction band edge is composed primarily of the B-site metal d-states, with some mixing indicative of covalency. Upon incorporation of the fist titanium atom into the supercell, the appearance of a new set of states primarily composed of titanium d-orbitals at the bottom of the conduction band is apparently responsible for the abrupt drop in the calculated band gap. As additional titanium atoms are incorporated, the density of these low-energy conduction band states increases proportionally, although the change in energy is smaller.

Different arrangements of the alloyed B-site ions had a minor effect on the calculated band gaps. For example, when the 12.5% Ti^{4+} case in an orthorhombic structure is considered, the lowest energy structure (with isolated Ti^{4+} ions) is only slightly lower in energy (~0.5 kJ/mol) than an alternative arrangement with linearly clustered Ti^{4+} ions; the bandgap of the latter was lower by approximately 50 meV (Figure 13). Despite the relatively small change, this suggests that inhomogeneities in the Ti^{4+} dopant distribution could contribute to the observed band-edge absorption broadening (increased Urbach energy) of the alloys, for instance as described by Nishigaki *et al.* for thin films of $BaZr_{1-x}Ti_xS_3$.[19]

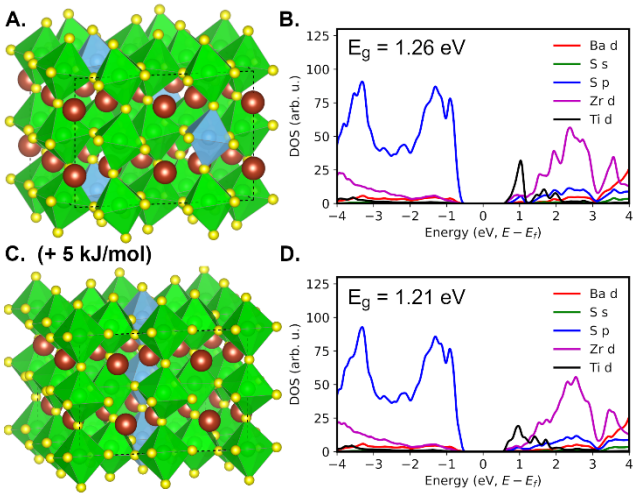

Figure 13. Changes in the partial density of states (PDOS) and band gap for structures with different Ti^{4+} dopant distributions, shown for the 12.5% Ti^{4+} case in the orthorhombic perovskite structure (corresponding 2 Ti ions out of 8 octahedral B-sites in the calculated supercell). (A) and (B) show the relaxed structure and PDOS plots for the lowest-energy calculated structure while (C) and (D) show the relaxed structure and PDOS plots for an alternative structure, higher in energy by 0.5 kJ/mol $BaMS_3$, with Ti^{4+} ions clustered in a 1D chain.

Conclusions

Overall, our study successfully demonstrated the solution-phase synthesis of Ti-alloyed $Ba(Zr_{1-x}Ti_x)S_3$ colloidal nanoparticles with a controllable titanium content, and the first reported synthesis of these alloyed materials by a method other than oxide sulfurization. Reactive metal amide precursors in oleylamine solvent facilitated the synthesis at temperatures at or below 300 °C. Ti-alloyed $Ba(Zr_{1-x}Ti_x)S_3$ nanoparticles underwent a phase transition from an orthorhombic to a hexagonal structure at titanium concentrations exceeding approximately x = 0.11, accompanied by a morphological shift from nanoplatelets to nanohexagons and nanobars. The optical property analysis revealed a reduction in the absorption onset of Ti-alloyed $Ba(Zr_{1-x}Ti_x)S_3$ nanocrystals and increased low-energy absorption, corresponding to a decreased band gap; high-Ti-content nanoparticles in the hexagonal phase exhibited near-IR absorption consistent with a transition to a low band-gap phase. Investigations into reaction time and temperature showed that $Ba(Zr_{1-x}Ti_x)S_3$ nanocrystals form within the first 10 minutes of the heat-up reaction at temperatures as low as 258 °C. Stability tests indicated that nanocrystals with higher titanium incorporation (x = 0.35) are less stable to ambient atmosphere than those with lower titanium content (x = 0.11), and both are somewhat less stable than the corresponding unalloyed phases. This study provides new potential pathways for the preparation of alloyed chalcogenide perovskite materials and new insights into the properties of group 4 transition metal chalcogenide nanomaterials with diverse compositions.

Conflicts of interest

There are no conflicts to declare.

Data availability

Data supporting this article has been included as part of the Supplementary Information.

Acknowledgements

This work was supported by the National Science Foundation of the United States (Grant #2004421 and Grant #2237082). Bruno Donnadieu is thanked for assistance with PXRD measurements and Dr. Roobanvenkatesh Thirulamai for assistance with TEM, EDX, and electron diffraction

measurements. Kasuni Handunge and Dr. Emily Tsui are thanked for acquiring XPS data at the University of Notre Dame Materials Characterization Facility. This work used Bridges-2 at the Pittsburgh Supercomputing Center through allocation CHE240014 from the Advanced Cyberinfrastructure Coordination Ecosystem: Servies & Supported (ACCESS) program,[63] which is supported by National Science Foundation grants #2138259, #2138286, #2138307, #2137603, and #2138296. KMM was supported by the NSF-INFEWS program at Mississippi State University (Grant #1852527).

~~The acknowledgements come at the end of an article after the conclusions and before the notes and references.~~

Notes and references

1 Interface engineering of highly efficient perovskite solar cells | Science, https://www.science.org/doi/full/10.1126/science.1254050, (accessed 22 August 2023).
2 Lead Iodide Perovskite Sensitized All-Solid-State Submicron Thin Film Mesoscopic Solar Cell with Efficiency Exceeding 9% | Scientific Reports, https://www.nature.com/articles/srep00591, (accessed 22 August 2023).
3 Organometal Halide Perovskites as Visible-Light Sensitizers for Photovoltaic Cells | Journal of the American Chemical Society, https://pubs.acs.org/doi/10.1021/ja809598r, (accessed 22 August 2023).
4 A. Kojima, K. Teshima, Y. Shirai and T. Miyasaka, *J. Am. Chem. Soc.*, 2009, **131**, 6050–6051.
5 Efficient planar heterojunction perovskite solar cells by vapour deposition | Nature, https://www.nature.com/articles/nature12509, (accessed 22 August 2023).
6 o-Methoxy Substituents in Spiro-OMeTAD for Efficient Inorganic–Organic Hybrid Perovskite Solar Cells | Journal of the American Chemical Society, https://pubs.acs.org/doi/full/10.1021/ja502824c, (accessed 22 August 2023).
7 Charge-Carrier Mobilities in Metal Halide Perovskites: Fundamental Mechanisms and Limits | ACS Energy Letters, https://pubs.acs.org/doi/full/10.1021/acsenergylett.7b00276, (accessed 22 August 2023).
8 Impact of microstructure on local carrier lifetime in perovskite solar cells | Science, https://www.science.org/doi/10.1126/science.aaa5333, (accessed 22 August 2023).
9 W. E. I. Sha, X. Ren, L. Chen and W. C. H. Choy, *Appl. Phys. Lett.*, 2015, **106**, 221104.
10 M. I. Alonso and M. Campoy-Quiles, in *Spectroscopic Ellipsometry for Photovoltaics: Volume 1: Fundamental Principles and Solar Cell Characterization*, eds. H. Fujiwara and R. W. Collins, Springer International Publishing, Cham, 2018, pp. 439–461.
11 Intrinsic Instability of Cs2In(I)M(III)X6 (M = Bi, Sb; X = Halogen) Double Perovskites: A Combined Density Functional Theory and Experimental Study | Journal of the American Chemical Society, https://pubs.acs.org/doi/full/10.1021/jacs.7b02227, (accessed 22 August 2023).
12 S. J. Adjogri and E. L. Meyer, *Materials*, 2021, **14**, 7857.
13 W. Meng, B. Saparov, F. Hong, J. Wang, D. B. Mitzi and Y. Yan, *Chem. Mater.*, 2016, **28**, 821–829.
14 K. V. Sopiha, C. Comparotto, J. A. Márquez and J. J. S. Scragg, *Adv. Opt. Mater.*, 2022, **10**, 2101704.
15 Y.-Y. Sun, M. L. Agiorgousis, P. Zhang and S. Zhang, *Nano Lett.*, 2015, **15**, 581–585.
16 T. Gupta, D. Ghoshal, A. Yoshimura, S. Basu, P. K. Chow, A. S. Lakhnot, J. Pandey, J. M. Warrender, H. Efstathiadis, A. Soni, E. Osei-Agyemang, G. Balasubramanian, S. Zhang, S. Shi, T. Lu, V. Meunier and N. Koratkar, *Adv. Funct. Mater.*, 2020, **30**, 2001387.
17 X. Wei, H. Hui, C. Zhao, C. Deng, M. Han, Z. Yu, A. Sheng, P. Roy, A. Chen, J. Lin, D. F. Watson, Y.-Y. Sun, T. Thomay, S. Yang, Q. Jia, S. Zhang and H. Zeng, *Nano Energy*, 2020, **68**, 104317.
18 Synthesis of BaZrS3 and BaHfS3 Chalcogenide Perovskite Films Using Single-Phase Molecular Precursors at Moderate Temperatures - Pradhan - 2023 - Angewandte Chemie International Edition - Wiley Online Library, https://onlinelibrary.wiley.com/doi/full/10.1002/anie.202301049, (accessed 22 August 2023).
19 Extraordinary Strong Band-Edge Absorption in Distorted Chalcogenide Perovskites - Nishigaki - 2020 - Solar RRL - Wiley Online Library, https://onlinelibrary.wiley.com/doi/10.1002/solr.201900555, (accessed 23 August 2023).
20 S. Niu, H. Huyan, Y. Liu, M. Yeung, K. Ye, L. Blankemeier, T. Orvis, D. Sarkar, D. J. Singh, R. Kapadia and J. Ravichandran, , DOI:10.48550/ARXIV.1804.09362.
21 X. Wei, H. Hui, S. Perera, A. Sheng, D. F. Watson, Y.-Y. Sun, Q. Jia, S. Zhang and H. Zeng, *ACS Omega*, 2020, **5**, 18579–18583.
22 S. Sharma, Z. Ward, K. Bhimani, K. Li, A. Lakhnot, R. Jain, S.-F. Shi, H. Terrones and N. Koratkar, *ACS Appl. Electron. Mater.*, 2021, **3**, 3306–3312.
23 A. Swarnkar, W. J. Mir, R. Chakraborty, M. Jagadeeswararao, T. Sheikh and A. Nag, *Chem. Mater.*, 2019, **31**, 565–575.
24 M. B. Kanoun, B. Ul Haq, A.-A. Kanoun and S. Goumri-Said, *Energy Fuels*, 2023, **37**, 9548–9556.
25 R. Yang, J. Nelson, C. Fai, H. A. Yetkin, C. Werner, M. Tervil, A. D. Jess, P. J. Dale and C. J. Hages, *Chem. Mater.*, 2023, **35**, 4743–4750.
26 M. Buffiere, D. S. Dhawale and F. El-Mellouhi, *Energy Technol.*, 2019, **7**, 1900819.
27 Untersuchungen über ternäre Chalkogenide. XI. Versuche zur Darstellung von Thioperowskiten - Hahn - 1957 - Zeitschrift für anorganische und allgemeine Chemie - Wiley Online Library, https://onlinelibrary.wiley.com/doi/abs/10.1002/zaac.19572880505, (accessed 23 August 2023).
28 A. Clearfield, *Acta Crystallogr.*, 1963, **16**, 135–142.
29 M. Surendran, H. Chen, B. Zhao, A. S. Thind, S. Singh, T. Orvis, H. Zhao, J.-K. Han, H. Htoon, M. Kawasaki, R. Mishra and J. Ravichandran, *Chem. Mater.*, 2021, **33**, 7457–7464.
30 C. Comparotto, A. Davydova, T. Ericson, L. Riekehr, M. V. Moro, T. Kubart and J. Scragg, *ACS Appl. Energy Mater.*, 2020, **3**, 2762–2770.
31 C. Comparotto, P. Ström, O. Donzel-Gargand, T. Kubart and J. J. S. Scragg, *ACS Appl. Energy Mater.*, 2022, **5**, 6335–6343.
32 A. A. Pradhan, M. C. Uible, S. Agarwal, J. W. Turnley, S. Khandelwal, J. M. Peterson, D. D. Blach, R. N. Swope, L. Huang, S. C. Bart and R. Agrawal, *Angew. Chem. Int. Ed.*, **n/a**, e202301049.

33 J. W. Turnley, K. C. Vincent, A. A. Pradhan, I. Panicker, R. Swope, M. C. Uible, S. C. Bart and R. Agrawal, *J. Am. Chem. Soc.*, 2022, **144**, 18234–18239.
34 H. W. Hillhouse and M. C. Beard, *Curr. Opin. Colloid Interface Sci.*, 2009, **14**, 245–259.
35 J.-H. Choi, H. Wang, S. J. Oh, T. Paik, P. Sung, J. Sung, X. Ye, T. Zhao, B. T. Diroll, C. B. Murray and C. R. Kagan, *Science*, 2016, **352**, 205–208.
36 D. Zilevu and S. E. Creutz, *Chem. Commun.*, 2023, **59**, 8779–8798.
37 Solution-phase synthesis of the chalcogenide perovskite barium zirconium sulfide as colloidal nanomaterials - Chemical Communications (RSC Publishing), https://pubs.rsc.org/en/content/articlelanding/2022/cc/d2cc03494h/unauth, (accessed 16 July 2023).
38 Detailed Balance Limit of Efficiency of p-n Junction Solar Cells | Journal of Applied Physics | AIP Publishing, https://pubs.aip.org/aip/jap/article-abstract/32/3/510/505950/Detailed-Balance-Limit-of-Efficiency-of-p-n?redirectedFrom=fulltext, (accessed 23 August 2023).
39 M. McQUARRIE and F. W. Behnke, *J. Am. Ceram. Soc.*, 1954, **37**, 539–543.
40 B. Okai, K. Takahashi, M. Saeki and J. Yoshimoto, *Mater. Res. Bull.*, 1988, **23**, 1575–1584.
41 D. Zilevu and S. E. Creutz, *Chem. Mater.*, 2021, **33**, 5137–5146.
42 S. Niu, G. Joe, H. Zhao, Y. Zhou, T. Orvis, H. Huyan, J. Salman, K. Mahalingam, B. Urwin, J. Wu, Y. Liu, T. E. Tiwald, S. B. Cronin, B. M. Howe, M. Mecklenburg, R. Haiges, D. J. Singh, H. Wang, M. A. Kats and J. Ravichandran, *Nat. Photonics*, 2018, **12**, 392–396.
43 B. A. Vaartstra, J. C. Huffman, W. E. Streib and K. G. Caulton, *Inorg. Chem.*, 1991, **30**, 121–125.
44 B. H. Toby and R. B. Von Dreele, *J. Appl. Crystallogr.*, 2013, **46**, 544–549.
45 E. B. Segal, *Chem. Health Saf.*, 2000, **7**, 18–23.
46 R. Yang, A. D. Jess, C. Fai and C. J. Hages, *J. Am. Chem. Soc.*, 2022, **144**, 15928–15931.
47 D. Zilevu, O. O. Parks and S. E. Creutz, *Chem. Commun.*, 2022, **58**, 10512–10515.
48 R. Lelieveld and D. J. W. IJdo, *Acta Crystallogr. B*, 1980, **36**, 2223–2226.
49 M. Saeki, M. Onoda and Y. Yajima, *J. Solid State Chem.*, 1996, **121**, 451–456.
50 J. Huster, *Z. Für Naturforschung B*, 1980, **35**, 775–775.
51 J. A. Brehm, J. W. Bennett, M. R. Schoenberg, I. Grinberg and A. M. Rappe, *J. Chem. Phys.*, 2014, **140**, 224703.
52 J. Jasieniak and P. Mulvaney, *J. Am. Chem. Soc.*, 2007, **129**, 2841–2848.
53 C. Morrison, H. Sun, Y. Yao, R. A. Loomis and W. E. Buhro, *Chem. Mater.*, 2020, **32**, 1760–1768.
54 R. Yang, A. D. Jess, C. Fai and C. J. Hages, *J. Am. Chem. Soc.*, , DOI:10.1021/jacs.2c06168.
55 S. Kong, H. Dong, Z. Yu, J. Guo, K. Cao, K. Chen, X. Ke, C. Zhou, J. Deng, S. Yang and Y. Zhang, *Ceram. Int.*, 2024, **50**, 10889–10896.
56 K. Okhotnikov, T. Charpentier and S. Cadars, *J. Cheminformatics*, 2016, **8**, 17.